Enhancement of topological magnon-driven spin currents through local edge strain in CrI_3 nanoribbons

David Sanz Ruiz [*] and David Soriano [†]
Departamento de Física Aplicada, Universidad de Alicante, 03690 Alicante, Spain

(Received 13 April 2026; accepted 1 July 2026; published 21 July 2026)

This work describes topological magnon transport in zigzag CrI_3 nanoribbons in the presence of edge strain. Exchange coupling terms under strain are obtained from first-principles calculations and the topological properties are introduced *via* second-neighbor Dzyaloshinskii-Moriya interactions (DMI). The magnon Hamiltonian is calculated using linear spin-wave theory and the Holstein-Primakoff transformation. Then, we use the nonequilibrium Green's function method to calculate the spin-wave-generated currents in ribbons with different edge strain. Our calculations show the formation of strongly localized edge topological magnons within the gap for DMI values slightly higher than the ones reported experimentally and in the presence of a tensile edge strain of the order of 3%. The magnon-mediated topological spin transport calculations show an increase of the spin current and characteristic decay length in tensile-strained CrI_3 nanoribbons compared with unstrained ones. Our findings demonstrate that straintronics provides a powerful route to harness and control topological magnons in two-dimensional magnetic materials.

DOI: 10.1103/lb9h-yb5j

I. INTRODUCTION

Magnetic two-dimensional (2D) materials have strongly revolutionized the fields of spintronics, allowing us to explore vibrant spin phenomena in few-nanometer-thick van der Waals heterostructures, ranging from ultrathin van der Waals magnetic tunnel junctions [1,2] to topological superconductivity [3]. A very appealing application of these materials resides in the transmission of information *via* electron spins by spin waves rather than electric currents, also known as insulator spintronics or low-power spintronics [4,5]. However, despite their considerable technological potential, ferromagnetic two-dimensional insulators have seen limited progress toward practical implementation in magnon-assisted spin transport. One of the primary limitations arises from the difficulty of detecting spin waves in ultrathin magnetic layers, where the reduced magnetic volume leads to significantly weaker signals compared to bulk materials such as yttrium iron garnet (YIG) [6].

Another notable property of some two-dimensional magnetic materials, including CrI_3 [7], is the appearance of topological magnon bands generated by spin-orbit-coupling-induced Kitaev [8] or second-neighbor Dzyaloshinskii-Moriya [9] interactions in hexagonal lattices. Neutron scattering experiments on bulk CrI_3 show a gapped spin-wave dispersion at K points [10], very similar to its fermionic homologous in hexagonal lattices [11]. Very important questions in this regard are how topological magnons can be detected in 2D ferromagnets [12] and which mechanisms can facilitate their detection.

Motivated by these questions and previous works on magnon straintronics [13], we use local edge strain to engineer the magnon spectrum of zigzag CrI_3 nanoribbons so that the topological magnon bands lie closer to thermally accessible energies near the magnon gap, thereby increasing their potential impact on spin transport and their experimental detectability. The paper is organized as follows. In Sec. II, we describe the methodology used throughout the manuscript (spin Hamiltonian, Holstein-Primakoff, nonequilibrium magnon transport, etc.). In Sec. III, we show the spin-wave dispersion of CrI_3 nanoribbons for different widths and in the presence and absence of second-neighbor Dzyaloshinskii-Moriya interactions (DMI). We demonstrate how transverse strain can tune the frequency of topological edge magnons, bringing them into the gap. In Sec. IV, we study the spin transport in strained CrI_3 nanoribbons mediated by spin waves using the nonequilibrium Green's function formalism as previously reported by Rückriegel *et al.* [14]. Finally, in Sec. V we discuss the results and report the main conclusions.

II. METHODOLOGY

A. Strain-dependent exchange interactions from DFT

Density functional theory (DFT) calculations were performed using the QUANTUM ESPRESSO *ab initio* package [15,16] to investigate exchange interactions in monolayer CrI_3 under various homogeneous strain conditions. The primary objective was to determine the exchange parameters as a function of strain, allowing for the generalization of this relationship to the nonhomogeneous strain profiles proposed for engineering magnon states.

We employed self-consistent spin-polarized DFT calculations within the generalized gradient approximation

[*]Contact author: sanzruiz999@gmail.com
[†]Contact author: david.soriano@ua.es

(GGA), using the Perdew-Burke-Ernzerhof (PBE) exchange-correlation functional [17] and the projector augmented wave (PAW) method [18]. Since we are interested in Heisenberg exchange terms, spin-orbit coupling (SOC) was excluded from these specific calculations. To account for electron-electron correlations and stabilize the ferromagnetic ground state of the CrI_3 monolayer, we applied the DFT $+ U + J$ scheme, incorporating both on-site Hubbard (U) and Hund's exchange (J) mean-field interactions. Specifically, we adopted values of $U = 2.7$ eV and $J = 0.7$ eV from Ref. [19]. For all the calculations, we used an $8 \times 8 \times 1$ k-point mesh, an energy convergence threshold of 10^{-9} Ry, and a lattice parameter of $a = 7.01$ Å.

We investigated the effect of in-plane biaxial strain in monolayer CrI_3 by distorting the lattice vectors within a range of $\pm 3\%$. For each strain configuration we calculated total energies of ferromagnetic and antiferromagnetic orders to establish a functional relationship between the exchange interactions and lattice distortions. The exchange interaction parameters were extracted by mapping the total energy differences between the ferromagnetic (FM) and antiferromagnetic (AFM) ground states to a nearest-neighbor spin Heisenberg model of the form

$$H = -\frac{1}{2}\sum_{ij} J_{ij}\mathbf{S}_i \cdot \mathbf{S}_j, \tag{1}$$

where J_{ij} represents the exchange coupling between nearest neighbors and S_i, S_j are spin vectors at i and j lattice sites. The general method to obtain exchange parameters directly from the total energies of *ab initio* calculations is to compare the FM and AFM energies (specifically a Néel AFM state), using the relation

$$J = \frac{E_{\mathrm{AFM}} - E_{\mathrm{FM}}}{2zS^2}, \tag{2}$$

where z is the neighbor coordination number. For the monolayer calculations used to extract the bulk parameter, $z = 3$.

The results of these calculations are presented in Fig. 1. For the unstrained system we find $J = 2.2$ meV, which is in good agreement with earlier reported results [19]. We observe an asymmetric response to the applied deformations: compressive strain has a stronger impact on the exchange interactions, decreasing the coupling, whereas tensile strain enhances the exchange interactions following a more moderate profile. These strain-dependent tendencies are consistent with recent first-principles studies [20,21].

We modeled the strain dependence of the magnetic exchanges between neighboring sites, $J(\varepsilon)$, using the exponential function

$$J(\varepsilon) = J_0(a - be^{-c\varepsilon}), \tag{3}$$

where the parameters a, b, and c are fitted to the DFT data as shown in Fig. 1(a). The strain parameter is defined by the local relative change in nearest-neighbor distances, $\varepsilon = \frac{a_0'}{a_0} - 1$. The exponential character of the strain dependence of J is physically motivated by the Cr-I-Cr superexchange mechanism [22–25], in which the exchange coupling $J \sim t^2/U$ inherits the exponential distance and bond angle of the Slater-Koster hopping integrals $t \propto e^{-(d-d_0)/\delta}$ [26], under biaxial strain.

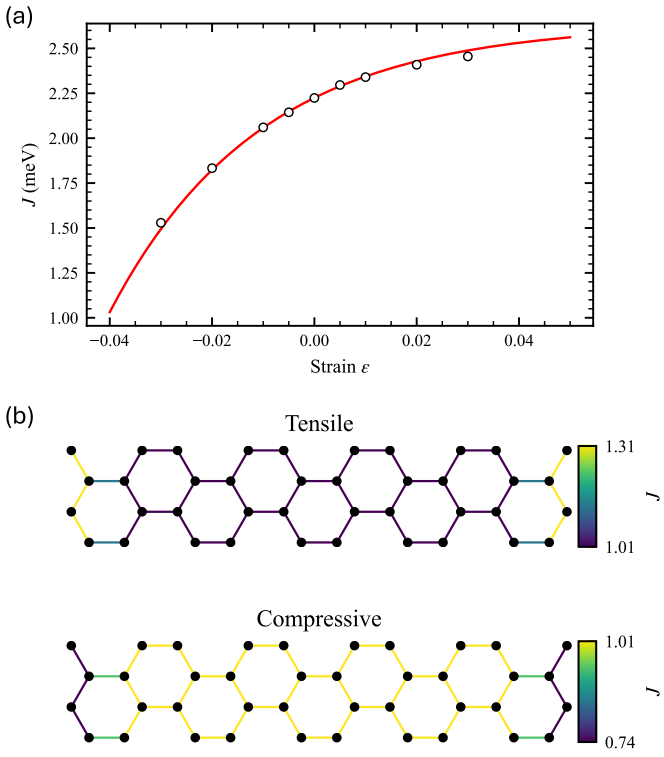

FIG. 1. (a) Nearest-neighbor exchange interactions obtained from *ab initio* DFT calculations (black dots) for a monolayer under homogeneous biaxial strain. The strain-dependent exchange coupling is interpolated using the phenomenological model $J(\varepsilon) = J_0(a - be^{-c\varepsilon})$ (red curve), with the unstrained exchange parameter $J_0 = 2.2$ meV and fitted parameters $a = 1.1987$, $b = 0.1874$, and $c = 33.9837$. The strain parameter is defined as $\varepsilon = a'/a - 1 = a_0'/a_0 - 1$, where a' (a_0') and a (a_0) denote the strained and unstrained lattice parameters (nearest-neighbor distances), respectively. (b) Spatial distribution of nearest-neighbor exchange interactions obtained by evaluating the fitted model locally in the presence of nonuniform strain field in units of J_0. The system is parametrized by a width $W = 10$, a smoothing length $\tau = a_0/4$, and strain amplitudes $\alpha_{\mathrm{str}} = -0.3$ and 0.6 Å.

This functional relationship allows us to introduce a nonuniform strain profile characterized by distortions localized at the edges of the ribbon. This approach exploits the imbalance in the coordination number between edges and bulk of nanoribbons, which enables the tuning of the magnons of the system. Specifically, we propose the following displacement field:

$$\Delta u_x = \alpha_{\mathrm{str}}(-e^{-(x-x_L)/\tau_{\mathrm{str}}} + e^{(x-x_R)/\tau_{\mathrm{str}}}), \tag{4}$$

where we introduce the parameter α_{str} that controls the amplitude of the lattice deformations, which is given in units of Å. The maximum strain value that will be applied for a fixed $\tau = a_0/4$ is given by $\sim \frac{\alpha_{\mathrm{str}}}{2a_0}$. x_L and x_R denote the left and right edge positions of the ribbons and τ (in units of a_0) modulates the spatial decay of the deformations.

Figure 1(b) illustrates the resulting exchange interactions under the proposed strain profile. Due to the asymmetric dependence of J with respect to ε [see Eq. (3)], compressive strains exert a stronger influence on magnon dynamics than

tensile strains. We restrict the applied deformation field to nearly the ranges explored in Fig. 1(a).

B. Spin-wave Hamiltonian of CrI_3 nanoribbon

In this work, we focus on the isotropic exchange interactions and its dependence on lattice deformations, extracted from DFT calculations. For this aim, we propose a Heisenberg model with second-neighbor DMI to describe the spin dynamics in CrI_3 nanoribbons. The system is modeled using the following spin Hamiltonian:

$$H = -\sum_{\langle ij\rangle} J_{ij}(\varepsilon)\boldsymbol{S}_i \cdot \boldsymbol{S}_j - \sum_{\langle ij\rangle} \lambda S_i^z S_j^z + \sum_{\langle\langle ij\rangle\rangle} \boldsymbol{D}_{ij} \cdot (\boldsymbol{S}_i \times \boldsymbol{S}_j) - \sum_i \boldsymbol{h}_i \cdot \boldsymbol{S}_i. \quad (5)$$

The first term is the nearest neighbor isotropic term with $\boldsymbol{S}_i$ being the spin operator associated with the i site and $J(_{ij}\epsilon)$ the strain-dependent Heisenberg exchange coupling, where the strain value is computed as the local change in the nearest-neighbor bond distance between sites i and j as $\varepsilon = \frac{d_{ij}}{d_0} - 1$, with d_0 the unstrained bond distance and d_{ij} the strained one. The second term contains the anisotropic exchange $\lambda = 0.1$ meV [19], which couples out-of-plane spins. The third term is the second-neighbor DMI which reflects the effect of the spin-orbit coupling (SOC) induced by the iodine ligands. $\boldsymbol{D}_{ij} = D\nu_{ij}$ is the antisymmetric DMI which captures clockwise hopping paths and encodes the system's topological characteristics [27]. The last term includes the effect of an external out-of-plane magnetic field. The DMI is fixed since the variation of the DMI vector under biaxial strain is negligible in comparison to that of J, as reported in prior DFT calculations [20].

The low energy spin excitations associated with the spin Hamiltonian in Eq. (5) are given in the form of quantized spin waves, i.e., magnons. We use linear spin-wave theory (LSWT) and the Holstein-Primakoff (HP) transformations to obtain the spin-wave Hamiltonian [28]:

$$S_i^+ \approx \sqrt{2S}a_i, \quad S_i^- \approx \sqrt{2S}a_i^\dagger, \quad S_i^z = S - a_i^\dagger a_i, \quad (6)$$

where $S_i^\pm = S_i^x \pm iS_i^y$ are the ladder spin operators at i site and $a_i^{(\dagger)}$ are the annihilation (creation) HP magnon operators. We apply HP only up to quadratic order and neglect higher ones related with magnon-magnon scattering interactions. The quadratic form of the LSWT Hamiltonian in real space H_{SW} is expressed as

$$H_{SW} = \sum_{ij}\left\{\delta_{ij}\left[\sum_n S(J_{in}(\epsilon) + \lambda_{in}) + h^{\text{ext}}\right] + T_{ij}\right\} a_i^\dagger a_j,$$
$$T_{ij} = -S(J_{ij}(\epsilon) + iD\nu_{ij}). \quad (7)$$

The strain-dependent exchange interaction is given by $J_{ij}(\varepsilon)$ for nearest-neighbor sites, while $\nu_{ij} = \pm 1$ determines the sign of the Dzyaloshinskii-Moriya interaction between next-nearest neighbors. The latter term is responsible for the emergence of nontrivial topological features in the magnon spectrum. The parameter λ_{ij} denotes the anisotropic exchange interaction between nearest neighbors and h^{ext} is an external magnetic field applied to stabilize the magnetic order.

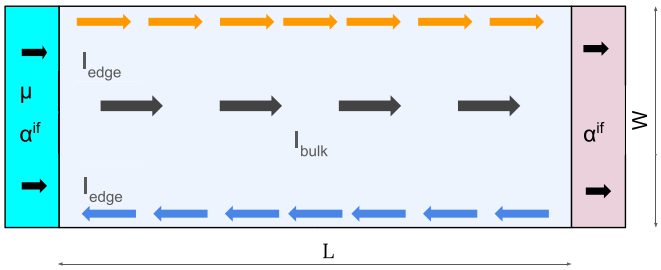

FIG. 2. Scheme of the transport device used for the simulation of magnon spin transport in nanoribbons. $\boldsymbol{\mu}$ represents the spin accumulation on the injecting lead on the left that couples to the spins of the ZNR manifested as an effective magnetic field. α^{if} represents the interfacial Gilbert damping that appears due to the contacts. Magnon modes excites at this edge propagate through the ZNR to the right side where the current is measured.

By applying periodic boundary conditions and performing a Fourier transform, the Hamiltonian in reciprocal space becomes

$$H_{SW} = \sum_k \sum_{ij}\left\{\delta_{ij}\left[\sum_n S(J_{in}(\epsilon) + \lambda_{in}) + h^{\text{ext}}\right] + T_{ij}(k)\right\} \times a_{k,i}^\dagger a_{k,j},$$
$$T_{ij}(k) = -S\left(J_{ij}(\epsilon) f_{ij}^{(1)}(k) + iD\nu_{ij} f_{ij}^{(2)}(k)\right), \quad (8)$$

where now i and j indices refer to sites within the unit cell; $f_{ij}^{(1)}(\mathbf{k}) = \sum_{\boldsymbol{\delta}_{ij}} e^{i\mathbf{k}\cdot\boldsymbol{\delta}_{ij}}$ and $f_{ij}^{(2)}(\mathbf{k}) = \sum_{\boldsymbol{\Delta}_{ij}} e^{i\mathbf{k}\cdot\boldsymbol{\Delta}_{ij}}$ denote the geometric structure factors resulting from the lattice vectors connecting nearest and next-nearest neighbors, respectively. It is worth noting that in Eq. (7) and Eq. (8) the on-site terms depend only on the local coordination number. In particular, for a bulk site in the nanoribbon $\epsilon_{\text{bulk}} = 3JS$, whereas for an edge site $\epsilon_{\text{edge}} = 2JS$.

Although the magnon Hamiltonian is structurally very similar to the standard tight-binding model of graphene [29], the magnon on-site terms originate from the exchange interaction and therefore depend on the local coordination number of each site. This difference between edge and bulk on-site terms leads to the disappearance of the flat band typically expected for zigzag graphene nanoribbons, as previously reported [8].

C. Nonequilibrium Green's function method for spin-wave transport

Having analyzed the impact of edge-localized strain on the magnon band structure, we now investigate its implications for the magnon transport in finite nanoribbons under different strains and DMI scenarios. For this purpose, we consider a finite nanoribbon connected to two nonmagnetic metallic leads as schematically illustrated in Fig. 2. The injecting lead generates a spin accumulation that couples exclusively to the interfacial spins of the zigzag CrI_3 nanoribbons (ZNR). This coupling is modeled as an effective magnetic field acting

on the contact sites. Additionally, thermal fluctuations are included to account for the stochastic excitation of magnon modes. Magnons propagate along the ribbon toward the opposite side, where the spin current is detected at the ejecting lead once the system reaches a steady-state regime.

We start by describing the dynamics of the magnetic moments using the stochastic Landau-Lifshitz-Gilbert (LLG) [30–32] equations, associated with each localized spin state in our nanoribbon systems as $\partial_t \boldsymbol{S}_i|_{\text{stoch}} = -\boldsymbol{S}_i \times \boldsymbol{h}_i^{\text{stoch}}$. The explicit expression becomes

$$\frac{\partial \boldsymbol{S}_i}{\partial t} = \mathbf{S}_i \times \left[-\frac{\partial H}{\partial \mathbf{S}_i} + \mathbf{h}_i^{\text{stoch}}(t) - \frac{\alpha_i}{S}\frac{\partial \boldsymbol{S}_i}{\partial t} + \frac{\alpha_i^{\text{if}}}{S}\mathbf{S}_i \times \boldsymbol{\mu}_i \right], \tag{9}$$

where $S = |\boldsymbol{S}_i|$ and H is the Heisenberg Hamiltonian from Eq. (5). The total phenomenological Gilbert damping at site i is $\alpha_i = \alpha + \alpha_i^{\text{if}}$, where α denotes the site-independent damping and α^{if} the interfacial damping that is nonzero only in the contact regions between the nanoribbon and the leads [33]. $\boldsymbol{\mu}_i$ describes the out-of-plane magnetic field that spins effectively "feel" in the nearby of the sites adjacent to the injecting lead. $\boldsymbol{h}_i^{\text{stoch}}(t)$ is the stochastic magnetic field that introduces thermal fluctuations by means of the dissipation-fluctuation theorem (FDT) and satisfies the conditions $\langle h_i^+(\omega)\rangle = 0$ and $\langle h_i^+(\omega)h_j^+(\omega')\rangle = 2\pi\delta_{ij}\delta(\omega-\omega')R_{ij}(\omega)$, where $h_i(\omega)$ is the Fourier transform of the circular component of the stochastic field $h_i^+ = h_i^x + ih_i^y$ and

$$R_i(\omega) = 4(\omega - \mu_i)\frac{\alpha_i}{S}n_B(\omega - \mu_i) \tag{10}$$

encodes the thermal magnon population [14,34,35], where $n_B(\omega)$ is the Bose-Einstein distribution.

We look for the solutions that consist of low-energy excitations of the ground state configuration relying on LSWT, i.e., magnons. To this end, we assume small transverse (in-plane) components S_i^x and S_i^y, corresponding to small deviations from the quantization axis. Under this assumption $S_i^z \approx S$ can be treated as constant, which allows one to linearize the LLG equations. The resulting equation of motion for $S_i^+ = S_i^x + iS_i^y$ is given by

$$i(1+i\alpha_i)\frac{\partial S_i^+}{\partial t} = \left[S\sum_j (J_{ij} + \lambda_{ij}) + h^{\text{ext}} \right] S_i^+ + \sum_j T_{ij}(\varepsilon)S_j^+ + Sh_i^+ - i\alpha_i^{\text{if}}\mu_i S_i^+, \tag{11}$$

where T_{ij} is the strain-dependent matrix element defined in Eq. (7).

Transforming Eq. (11) into frequency domain allows us to define the system's Green's function of the system, with the stochastic magnetic field acting as an external source,

$$G_{ij}^{-1}(\omega) = \delta_{ij}\left[-(1+i\alpha_i)\omega + \sum_j S(J_{ij} + \lambda_{ij}) + i\alpha_i^{\text{if}} S\mu_i \right] + T_{ij}, \tag{12}$$

with T_{ij} the matrix element of the LSWT Hamiltonian defined in Eq. (7). After normalizing the spin operator, the formal solution can be formulated in terms of this Green's function and the stochastic field $h_i^+(\omega)$ as the external source:

$$\sum_j G_{ij}^{-1}(\omega)S_j^+(\omega) = h_i^+(\omega). \tag{13}$$

The spin current can be established by looking at the steady state regime of the system, which is governed by the expectation value of the equation of motion of the S_i^z component. The steady state is achieved by the condition $\langle S_i^z\rangle = 0$. Substituting the formal solution Eq. (13) in the equation of motion for the S_i^z in Eq. (11), we arrive at the final expression:

$$\left\langle \sum_j T_{ij}\text{Im}[S_i^- S_j^+] \right\rangle = -\langle \alpha_i \text{Im}[S_i^- \partial_t S_i^+] - \text{Im}[h_i^- S_i^+] - \alpha_i^{\text{if}}\mu_i S_i^+ S_i^- \rangle. \tag{14}$$

Here, the term on the left represents the spin current between nearest neighbors i and j mediated by the exchange interaction. On the right, we identify the spin current drain source due to the Gilbert damping term, alongside the injecting sources driven by the thermal heat bath, modeled by h_i^+, and the spin accumulation μ_i located at the contact regions between the ribbon and the leads. Based on Eq. (14), we define the aforementioned spin current terms acting on site i as

$$\sum_j \langle I_{i\to j}\rangle = \langle I_i^{\alpha}\rangle + \langle I_i^{\text{stoch}}\rangle + \langle I_i^{\mu}\rangle. \tag{15}$$

Using the solution of Eq. (13) in the right side of Eq. (14), we find that the total injected spin current at the end of the nanoribbon is

$$I = \sum_{i\in\text{frontier}} \text{Im}\int \frac{d\omega}{2\pi}\,[STG(\omega)R(\omega)G^{\dagger}(\omega)]_{ii}, \tag{16}$$

with I the total integrated spin current at the ejection zone of the ZNR, $R(\omega)$ the encoding thermal fluctuations from the stochastic field in Eq. (10), i the lattice positions where we measure the spin current, and T the hopping matrix of the LSWT magnon model as in Eq. (7). $G(\omega)$ can be computed through the inversion of Eq. (12). The total ejected spin current can be separated by energy windows; hence, separating states in the magnon gap near the crossing point of the chiral bands from the bulk states located below that gap, we can study the behavior of topological edge states in spin transport and its response to the proposed strain.

III. EFFECT OF LOCAL EDGE STRAIN IN MAGNON DISPERSION

We investigate the strain-induced modifications of the magnetic exchange interactions by applying an edge-localized strain to the ZNR system. The ZNR is characterized by its width (W), defined as the number of zigzag chains across the transverse direction of the ribbon. The system is assumed to be periodic along the ribbon axis and finite along the transverse direction, resulting in a one-dimensional Brillouin zone for the longitudinal momentum (k). The band structure is obtained from the LSWT Hamiltonian defined in Eq. (8). This strain profile is designed to tune the imbalance between edge and bulk coordination environments, thereby interpolating between the ideal LSWT honeycomb limit and the

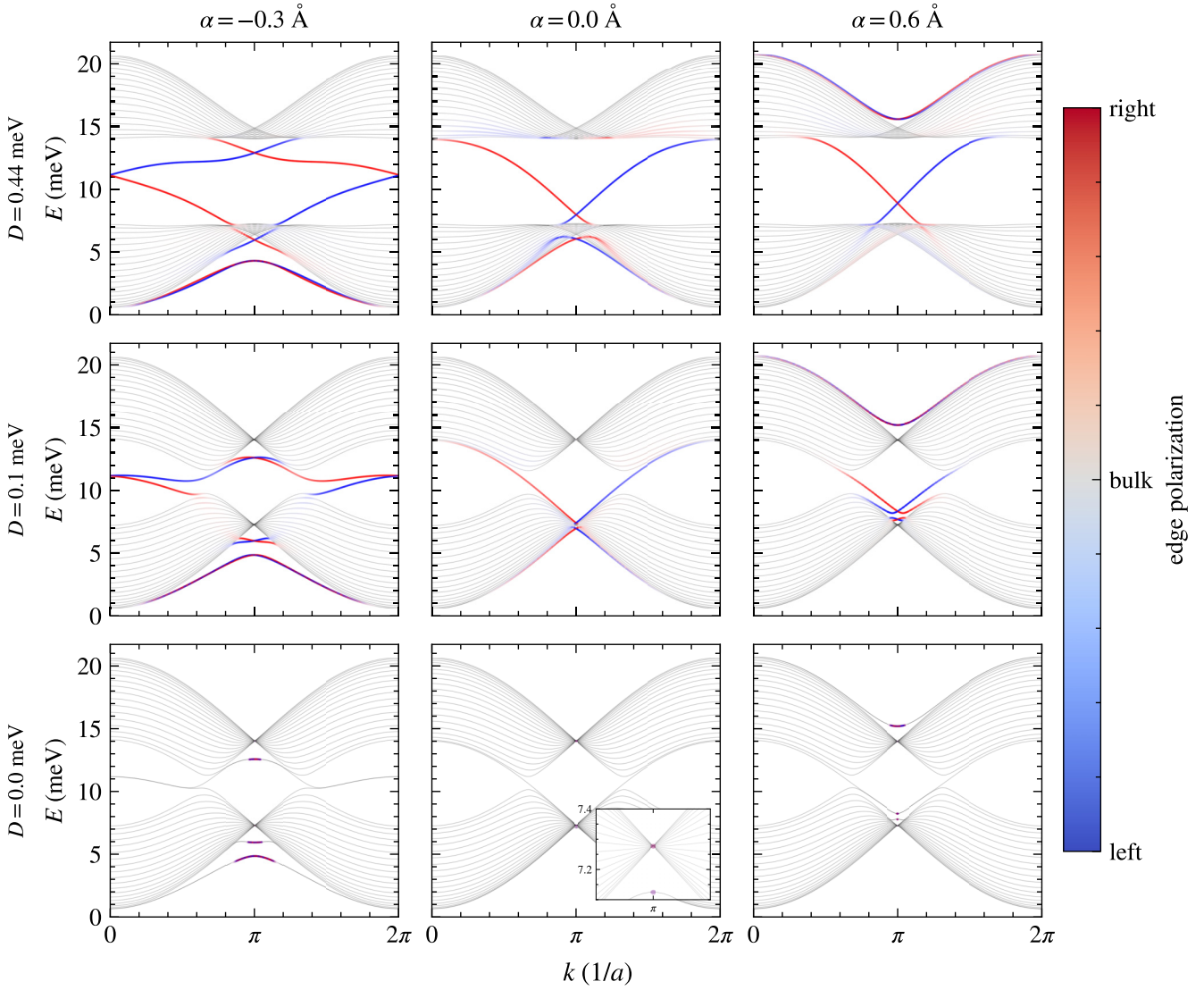

FIG. 3. Magnon dispersion relation of a $W = 20$ ZNR for different strain values $\alpha = -0.3, 0.0, 0.6$ Å, with fixed $\tau = a_0/4$, and different DMI values $D = 0$ meV (bottom row), $D = 0.1$ meV (middle row), and $D = 0.44$ meV (top row), along k path $k \in [0, \frac{2\pi}{a}]$. Fixed parameters $J = 2.2$ meV, $\lambda = 0.1$ meV, $h_{\text{ext}} = 0.1$ meV, and $S = 3/2$. We have picked up the four outermost sites from both edges (blue: left; red: right; gray: bulk) of the ZNR to compute the wave function weights associated to each edge as $|c_n(k)|^2 = \sum_{i\in\text{left (right)}} |M_{in}(k)|^2$.

graphenelike edge-band regime. To this end, we employ the strain dependence of the magnetic exchange from Eq. (3) with the displacement field introduced in Eq. (4), where the parameters were fitted to the DFT results shown in Fig. 1.

Figure 3 shows the magnon dispersion relations resulting from the application of a nonuniform strain for increasing values of the DMI and a range of strain intensities α_{str}. To distinguish between edge and bulk states, bands are highlighted in red (blue) according to the magnon eigenstate weights projected onto the outermost A-sublattice (B-sublattice) and second-row B-sublattice (A-sublattice) sites of the left (right) edge. In particular, we use the eigenstate weights $|c_n(k)|^2 = \sum_{i\in\text{left (right)}} |M_{in}(k)|^2$.

The central column corresponds to the case without strain, while the left and right columns show the dispersion relations for compressive and tensile strain, respectively. Considering that second neighbor DMI values obtained from inelastic neutron scattering experiments of bulk CrI_3 are of the order of 0.3 meV [10], we have studied three different cases: trivial ZNR with $D = 0$ meV (bottom panel), a ZNR with $D = 0.1$ meV, a DMI smaller than the one predicted experimentally (middle panel), and a ZNR with $D = 0.44$ meV, a DMI slightly higher than the experimental one (top panel).

In the absence of strain ($\alpha = 0.0$ Å) and DMI ($D = 0$ meV), there is a negligible presence of trivial edge states at $k = \pi$ (see small purple projection in the bottom central panel, which results from the superposition of left and right weights), which comes from the zigzag nature of the ribbon edge, very similar to the fermionic case [36,37]. However, the imbalance in magnon on-site energies, which differ between edge and bulk sites due to the reduced coordination numbers at the edges, shift the energy of these states to

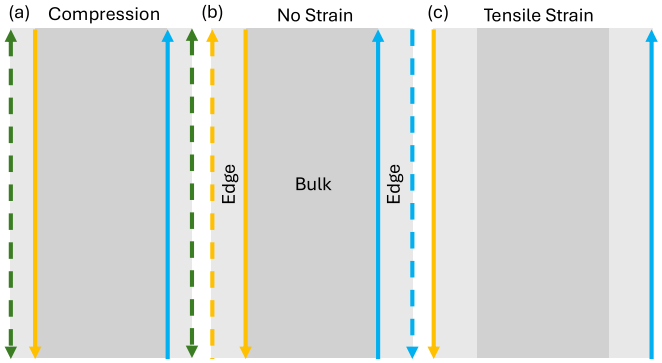

FIG. 4. Schematics of the magnon edge state formation for CrI_3 nanoribbons under (a) compression, (b) no strain, and (c) tensile strain. The light gray regions represent the edge, containing inner (close to the bulk) and outer sites. The dashed arrows correspond to the second magnon edge state. Orange (blue) arrows correspond to left (right) edge magnon states. We have used green to denote nonchiral edge magnon states.

lower values, around ∼7 meV. In the case of a small DMI ($D = 0.1$ meV) a topological spin-wave gap between optical and acoustic magnon branches of $\Delta_{SW} = 1.85$ meV appears. Here, the topological magnon gap refers to the value obtained by diagonalizing Eq. (8) for monolayer CrI_3. The nontrivial edge states located at $E \sim 7$ meV for $D = 0.1$ meV split into two copies with opposite chirality (see the middle central panel). The lower energy chiral edge states come from the outer sites of the edge which present a lower coordination leading to a slightly smaller on-site energy. The chiral states with higher energy correspond to the inner edge sites which conserve the coordination number of the two-dimensional system [see Fig. 4(b)]. The top central panel shows the case with strong DMI ($D = 0.44$ meV), the magnon gap increases to $\Delta_{SW} = 6.68$ meV, and the nontrivial edge states with opposite chirality show a higher splitting. While the excitation energies of the lower pair lie at values similar to the lower bulk manifold, making difficult its characterization, the upper pair is completely isolated in the gap and shows a high linear dispersion.

Applying compressive strain in the edge ($\alpha = -0.3$ Å) reduces the exchange interaction as shown in Fig. 1, lowering even more the on-site energy of the edge magnons. For $D = 0$ meV, this leads to the emergence of localized magnon edge states appearing at lower energies (see Fig. 3, bottom left). These low energy states ($E < 7$ meV) are localized in the outer and inner sublattice edge sites, respectively. In contrast to the $\epsilon = 0$ case, here the splitting corresponding to the pair of edge states is clearly visible due to the strain inducing a higher energy difference between the outer and inner sites, which leads to the emergence of quasiflat bands between the acoustic and optical magnon branches. The higher energy band showing edge projection shows a combination of inner and outer edge sites. For $D = 0.1$ meV (middle left panel), the lower energy bands belonging to the outer edge sites do not show any chirality (red and blue edge projections overlap). The other two bands become chiral with crossing points at $k = \pi/a$ and opposite chirality [see Fig. 4(a)]. Increasing the DMI ($D = 0.44$ meV), the magnon bands show a similar structure compared to the $D = 0.1$ meV case. However, the increase of the DMI induces a higher dispersion of the chiral edge states and increases the topological gap allowing the observation of the higher energy chiral edge bands (Fig. 3, top left panel).

In the tensile regime ($\alpha = 0.6$ Å), the exchange interaction is increased near the edge. However, since the tensile strain affects less the value of the Heisenberg exchange coupling between Cr atoms (see Fig. 1), it is expected that the magnon dispersion will be slightly modified with respect to the case without strain. For $D = 0$ meV (Fig. 3, right bottom panel), the magnon dispersion shows three states around $k = \pi/a$, which are localized at the edges. In this case, the outermost sites contribute mainly to the central edge band, while the low-energy and high-energy bands have contributions from the inner and bulk sites. For $D = 0.1$ meV, the first two edge bands become chiral, while the third one at high energy shows no chirality. The combination of tensile strain and higher DMI (Fig. 3, top right panel) gives rise to a pair of chiral localized edge states completely isolated inside the gap coming from the outer edge sites [see Fig. 4(c)]. The low energy chiral edge state, visible for $D = 0.1$ meV, hybridizes completely with the bulk states and disappears.

IV. MAGNON-MEDIATED SPIN TRANSPORT IN CrI_3 NANORIBBONS

After analyzing the impact of the local strain on the magnon band structure, we focus now on the study of its impact on the magnon transport properties by considering the device depicted in Fig. 2 for a nanoribbon with fixed width $W = 8$. We investigate the decay of spin currents by varying the ribbon length l. In all simulations, Anderson disorder is modeled by incorporating randomly distributed large on-site energy perturbations with a concentration of $w_{deff} = 15\%$ relative to the total number of lattice sites. The spin currents are computed using the relaxation LLG-LSWT formalism [Eq. (16)], where the Green's functions are constructed from the LSWT Hamiltonian incorporating the strain model defined in Eq. (3) and Eq. (4). We focus specifically on the strong DMI regime ($D = 0.44$ meV), as our previous band structure analysis (Fig. 3) demonstrated that this regime effectively isolates the topological edge states within the band gap and shows higher band dispersion.

Figures 5(a)–5(c) present the magnitude of the calculated edge (orange) and bulk (blue) spin currents I as a function of length for three representative strain amplitudes. As expected for a disordered system, we observe a clear exponential suppression of the spin current, following $I(l) \propto e^{-l/\lambda}$. Notably, the edge contribution consistently dominates the transport, exhibiting a slower decay than the bulk, which confirms the topological protection of the edge modes even in the presence of significant disorder.

A comparison of the panels shows that the decay length is highly sensitive to the applied strain. This dependence is quantified in Fig. 5(d), where the characteristic decay length λ is plotted as a function of the strain amplitude α_{str}. The data exhibit a monotonic increase of λ with α_{str}: under compressive

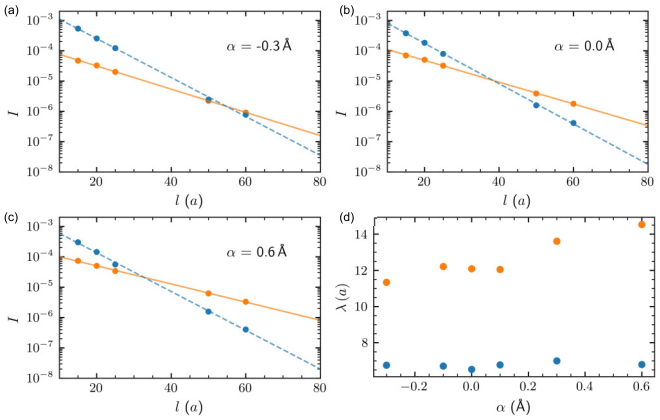

FIG. 5. Spin currents ejected as a function of the ribbon length l and strain amplitude α. The simulation parameters are fixed at $J = 2.2$ meV, $J_{\text{ani}} = 0.1$ meV, $D = 0.44$ meV, $h_{\text{ext}} = 0.1J$, and $T = 0.8J$, with a defect concentration of 15%. (a)–(c) Spin currents for compressive ($\alpha = -0.3$ Å), zero, and tensile ($\alpha = 0.6$ Å) strain. Orange (blue) markers represent the edge (bulk) spin current contributions. Dashed lines indicate the exponential fits $I(l) \propto e^{-l/\lambda}$. (d) Characteristic decay length λ as a function of the strain parameter α, extracted from the fits.

strain ($\alpha < 0$) spin transport is strongly suppressed, producing short edge decay lengths ($\lambda_{\text{edge}} \sim 11a$), whereas tensile strain ($\alpha > 0$) extends the transport range, raising λ_{edge} to $\sim 14a$ at $\alpha = 0.6$ Å. As for the bulk currents, strain does not have a great impact on its decay lengths $\lambda_{\text{bulk}} \sim 7.5a$. To explain this behavior, we need to compare with the magnon band dispersions obtained in the previous section. It is important to note that low-energy magnon states contribute significantly more to the overall spin transport than high-energy ones. This occurs because the thermal occupation of high-energy modes is exponentially suppressed at lower temperatures, as dictated by the Bose-Einstein distribution (see Supplemental Material [38] for further details about the thermal modulation of occupations). For this reason we focus on bands with $E < 10$ meV. We see a clear trend, namely, the decay length of the spin currents mediated by topological magnons increases as the crossing point (or critical point) of the topologically protected magnon edge bands shifts towards the gap. This clearly pinpoints the importance of edge strain to decouple edge transport and bulk transport in order to maximize spin currents in 2D ferromagnetic insulators.

V. CONCLUSIONS

In this work, we have theoretically investigated the manipulation of magnon transport in monolayer CrI_3 zigzag nanoribbons through the application of edge-localized strain. By combining first-principles DFT calculations with linear spin wave theory (LSWT) and Green's function transport simulations, we have established a direct link between mechanical deformation, magnetic exchange modulation, and the robustness of spin currents. We have demonstrated that mechanical deformation can control the localization of the topological magnon states at the edges, thereby providing a new platform for manipulating localization in specific sublattices and shifting these states to lower or higher energies.

In the trivial DMI regime ($D = 0$), we showed that compressive strain restores localized edge states that are otherwise absent due to the edge-bulk energy mismatch. Conversely, in the topological regime (finite DMI), strain acts as a powerful control knob for the chiral edge modes. We found that while compressive strain tends to hybridize the topological states with the bulk manifold, tensile strain lifts the chiral edge states allowing one to isolate them within the gap, allowing for a potential characterization.

Finally, our transport calculations in disordered ribbons provided quantitative evidence of these topological protection mechanisms. We observed that the characteristic decay length of the spin current (λ) is strongly modulated by the applied strain field. Specifically, tensile strain significantly enhances the transport range ($\lambda \approx 14a$) by protecting the chiral edge channels from scattering into the bulk. In contrast, compressive strain reduces the decay length ($\lambda \approx 11a$) by promoting edge-bulk hybridization.

These findings highlight the potential of magnon straintronics as a viable route for engineering robust, dissipationless spin transport channels in two-dimensional magnetic materials. The ability to mechanically tune the topological properties of magnons without altering the chemical composition paves the way for developing flexible and energy-efficient spintronic devices.

ACKNOWLEDGMENTS

D.S. and D.S.R. acknowledge financial support from Generalitat Valenciana through the CIDEGENT program (CIDEGENT/2021/052) and the Advanced Materials program by MCIN with funding from European Union NextGenerationEU (MFA/2022/045).

DATA AVAILABILITY

The data that support the findings of this article are not publicly available upon publication because it is not technically feasible and/or the cost of preparing, depositing, and hosting the data would be prohibitive within the terms of this research project. The data are available from the authors upon reasonable request.

[1] D. R. Klein, D. MacNeill, J. L. Lado, D. Soriano, E. Navarro-Moratalla, K. Watanabe, T. Taniguchi, S. Manni, P. Canfield, J. Fernández-Rossier, and P. Jarillo-Herrero, Probing magnetism in 2D van der Waals crystalline insulators via electron tunneling, Science **360**, 1218 (2018).

[2] Z. Wang, I. Gutiérrez-Lezama, N. Ubrig, M. Kroner, M. Gibertini, T. Taniguchi, K. Watanabe, A. Imamoğlu, E. Giannini, and A. F. Morpurgo, Very large tunneling magnetoresistance in layered magnetic semiconductor CrI_3, Nat. Commun. **9**, 2516 (2018).

[3] S. Kezilebieke, M. N. Huda, V. Vaňo, M. Aapro, S. C. Ganguli, O. J. Silveira, S. Głodzik, A. S. Foster, T. Ojanen, and P. Liljeroth, Topological superconductivity in a van der Waals heterostructure, Nature (London) **588**, 424 (2020).

[4] A. V. Chumak, V. I. Vasyuchka, A. A. Serga, and B. Hillebrands, Magnon spintronics, Nat. Phys. **11**, 453 (2015).

[5] S. Mañas-Valero, T. van der Sar, R. A. Duine, and B. van Wees, Fundamentals and applications of van der Waals magnets in magnon spintronics, Newton **1**, 100018 (2025).

[6] X. Y. Wei, O. A. Santos, C. H. S. Lusero, G. E. W. Bauer, J. Ben Youssef, and B. J. van Wees, Giant magnon spin conductivity in ultrathin yttrium iron garnet films, Nat. Mater. **21**, 1352 (2022).

[7] B. Huang, G. Clark, E. Navarro-Moratalla, D. R. Klein, R. Cheng, K. L. Seyler, D. Zhong, E. Schmidgall, M. A. McGuire, D. H. Cobden, *et al.*, Layer-dependent ferromagnetism in a van der Waals crystal down to the monolayer limit, Nature (London) **546**, 270 (2017).

[8] E. Aguilera, R. Jaeschke-Ubiergo, N. Vidal-Silva, L. E. F. F. Torres, and A. S. Nunez, Topological magnonics in the two-dimensional van der Waals magnet CrI_3, Phys. Rev. B **102**, 024409 (2020).

[9] A. T. Costa, D. L. R. Santos, N. M. R. Peres, and J. Fernández-Rossier, Topological magnons in CrI_3 monolayers: An itinerant fermion description, 2D Mater. **7**, 045031 (2020).

[10] L. Chen, J.-H. Chung, B. Gao, T. Chen, M. B. Stone, A. I. Kolesnikov, Q. Huang, and P. Dai, Topological spin excitations in honeycomb ferromagnet CrI_3, Phys. Rev. X **8**, 041028 (2018).

[11] C. L. Kane and E. J. Mele, Quantum spin Hall effect in graphene, Phys. Rev. Lett. **95**, 226801 (2005).

[12] J. Zhang, M.-H. Zhang, P. Li, Z. Liu, Y. Tao, H. Wang, D.-X. Yao, D. Guo, and D. Zhong, Observation of topological magnon edge states, ACS Nano **20**, 700 (2026).

[13] D. L. Esteras, A. Rybakov, A. M. Ruiz, and J. J. Baldoví, Magnon straintronics in the 2D van der Waals ferromagnet CrSBr from first-principles, Nano Lett. **22**, 8771 (2022).

[14] A. Rückriegel, A. Brataas, and R. A. Duine, Bulk and edge spin transport in topological magnon insulators, Phys. Rev. B **97**, 081106(R) (2018).

[15] P. Giannozzi, S. Baroni, N. Bonini, M. Calandra, R. Car, C. Cavazzoni, D. Ceresoli, G. L. Chiarotti, M. Cococcioni, I. Dabo, A. Dal Corso, S. de Gironcoli, S. Fabris, G. Fratesi, R. Gebauer, U. Gerstmann, C. Gougoussis, A. Kokalj, M. Lazzeri, L. Martin-Samos, *et al.*, Quantum ESPRESSO: A modular and open-source software project for quantum simulations of materials, J. Phys.: Condens. Matter **21**, 395502 (2009).

[16] P. Giannozzi, O. Andreussi, T. Brumme, O. Bunau, M. Buongiorno Nardelli, M. Calandra, R. Car, C. Cavazzoni, D. Ceresoli, M. Cococcioni, N. Colonna, I. Carnimeo, A. Dal Corso, S. de Gironcoli, P. Delugas, R. A. DiStasio, A. Ferretti, A. Floris, G. Fratesi, G. Fugallo, *et al.*, Advanced capabilities for materials modelling with QUANTUM ESPRESSO, J. Phys.: Condens. Matter **29**, 465901 (2017).

[17] A. Dal Corso, Pseudopotentials periodic table: From H to Pu, Comput. Mater. Sci. **95**, 337 (2014).

[18] P. E. Blöchl, Projector augmented-wave method, Phys. Rev. B **50**, 17953 (1994).

[19] J. L. Lado and J. Fernández-Rossier, On the origin of magnetic anisotropy in two dimensional CrI_3, 2D Mater. **4**, 035002 (2017).

[20] M. Soenen and M. V. Milošević, Tunable magnon topology in monolayer CrI_3 under external stimuli, Phys. Rev. Mater. **7**, 084402 (2023).

[21] L. Webster and J.-A. Yan, Strain-tunable magnetic anisotropy in monolayer $CrCl_3$, $CrBr_3$, and CrI_3, Phys. Rev. B **98**, 144411 (2018).

[22] P. W. Anderson, Antiferromagnetism. Theory of superexchange interaction, Phys. Rev. **79**, 350 (1950).

[23] P. W. Anderson, New approach to the theory of superexchange interactions, Phys. Rev. **115**, 2 (1959).

[24] K. W. Song and V. I. Fal'ko, Superexchange and spin-orbit coupling in monolayer and bilayer chromium trihalides, Phys. Rev. B **106**, 245111 (2022).

[25] Y. O. Kvashnin, A. Bergman, A. I. Lichtenstein, and M. I. Katsnelson, Relativistic exchange interactions in CrX_3 (X = Cl, Br, I) monolayers, Phys. Rev. B **102**, 115162 (2020).

[26] J. C. Slater and G. F. Koster, Simplified LCAO method for the periodic potential problem, Phys. Rev. **94**, 1498 (1954).

[27] S. A. Owerre, A first theoretical realization of honeycomb topological magnon insulator, J. Phys.: Condens. Matter **28**, 386001 (2016).

[28] T. Holstein and H. Primakoff, Field dependence of the intrinsic domain magnetization of a ferromagnet, Phys. Rev. **58**, 1098 (1940).

[29] A. H. C. Neto, F. Guinea, N. M. R. Peres, K. S. Novoselov, and A. K. Geim, The electronic properties of graphene, Rev. Mod. Phys. **81**, 109 (2009).

[30] L. D. Landau and E. M. Lifshitz, On the theory of the dispersion of magnetic permeability in ferromagnetic bodies, Phys. Z. Sowjetunion **8**, 153 (1935).

[31] T. L. Gilbert, A phenomenological theory of damping in ferromagnetic materials, IEEE Trans. Magn. **40**, 3443 (2004).

[32] W. F. Brown, Thermal fluctuations of a single-domain particle, Phys. Rev. **130**, 1677 (1963).

[33] Y. Tserkovnyak, A. Brataas, and G. E. W. Bauer, Enhanced Gilbert damping in thin ferromagnetic films, Phys. Rev. Lett. **88**, 117601 (2002).

[34] S. A. Bender, H. Skarsvåg, A. Brataas, and R. A. Duine, Enhanced spin conductance of a thin-film insulating antiferromagnet, Phys. Rev. Lett. **119**, 056804 (2017).

[35] A. Brataas, H. Skarsvåg, E. G. Tveten, and E. L. Fjærbu, Heat transport between antiferromagnetic insulators and normal metals, Phys. Rev. B **92**, 180414(R) (2015).

[36] K. Nakada, M. Fujita, G. Dresselhaus, and M. S. Dresselhaus, Edge state in graphene ribbons: Nanometer size effect and edge shape dependence, Phys. Rev. B **54**, 17954 (1996).

[37] K. Wakabayashi, K.-i. Sasaki, T. Nakanishi, and T. Enoki, Electronic states of graphene nanoribbons and analytical solutions, Sci. Technol. Adv. Mater. **11**, 054504 (2010).

[38] See Supplemental Material at http://link.aps.org/supplemental/10.1103/lb9h-yb5j for detailed derivations of the magnon decay dependence on excitation energy, thermal modulation of magnon excitations, spin current decomposition, and extended data for the moderate DMI regime.